

Coupled dynamical phase transitions in driven disk packings

Akash Ghosh,¹ Jaikumar Radhakrishnan,² Paul M. Chaikin,³ Dov Levine,⁴ and Shankar Ghosh¹

¹*Dept. of Condensed Matter Physics and Materials Science, Tata Institute of Fundamental Research, Mumbai 400005, India*

²*School of Technology and Computer Science, Tata Institute of Fundamental Research, Mumbai 400 005, India*

³*Center for Soft Matter Research and Department of Physics, New York University, New York, NY 10003*

⁴*Department of Physics, Technion-IIT, Haifa 32000, Israel*

(Dated: March 15, 2022)

Under the influence of oscillatory shear, a mono-layer of frictional granular disks exhibits two dynamical phase transitions: a transition from an initially disordered state to an ordered crystalline state, and a dynamic active-absorbing phase transition. Although there is no reason, *a-priori*, for these to be at the same critical point, they are. The transitions may also be characterized by the disk trajectories, which are non-trivial loops breaking time-reversal invariance.

Dynamical phase transitions between active and absorbing states have been a paradigm in non-equilibrium physics for some time [1, 2]. On one side of the transition the system is dynamic, where a fraction α of the particles are “active”, and move continually. On the other side, all motion ceases. Typically, this cessation of dynamics occurs when the constituent particles achieve some local goal, such as becoming non-overlapping, or having no near neighbors. The transition is characterized by a critical point at which long-range correlations are manifested, but the critical state is typically disordered and hyperuniform [3], as has been shown [4] for systems in the conserved directed percolation (or Manna) class [1]. Such a transition has been studied in a variety of models theoretically [1], and experimentally in a system of non-Brownian hard spheres suspended in a viscous fluid [5–7]. For these systems, the fraction α of active particles is the order parameter for the transition: in the absorbing phase, $\alpha = 0$; in the active phase $\alpha > 0$.

Many of these investigations involve studying disordered systems under cyclic shear [8–19], where the absorbing phase is linked to the system’s elastic response and the commencement of the active phase is related to yielding phenomena [10–13, 20, 21]. In this phase the constituent particles can exhibit interesting limit cycle dynamics [8, 9, 22]. Such continued cyclic shearing can modify the yielding transition [10, 23] and even encode the memory of the training process [8, 14–16].

In this paper, we report our findings from experiments performed with a collection of frictional disks that are subjected to oscillatory shear. The system, depicted in Fig. 1, consists of a single layer of identical disks confined between glass plates which are inclined with respect to the normal. The disks interact frictionally with one another as well as with the bottom plate. In addition, they experience gravity, as a result of which there is a pressure gradient in the system [24]. As we will detail presently, for large strain the system may be regarded as being in an active state, where a fraction of the disks do not return to their positions after a strain cycle. For small strain, the system goes to an absorbing state, where all the disks return to their initial positions. The system,

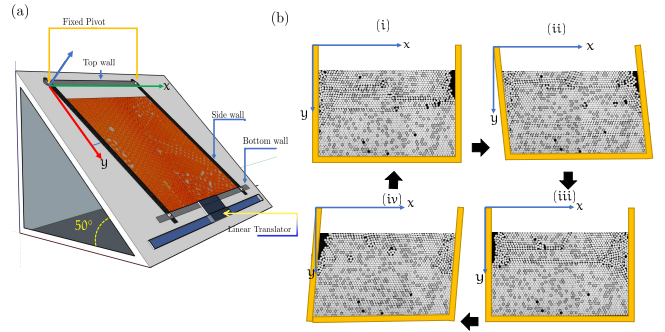


FIG. 1. (a) Schematic of the apparatus. All the walls of the shear cell are about 53 particle diameters long. (b) One cycle: The sequence (i) \rightarrow (ii) \rightarrow (iii) \rightarrow (iv) \rightarrow (iv) \rightarrow (i) completes one shear cycle. The sequence starts from the “zero position” (i), moving to the rightmost position (ii), returning to the central position (iii), then moving on to the leftmost position (iv) before finally coming back to the zero position.

however, is typically not homogeneous, with the upper portion becoming active before the lower part. This suggests that pressure is also a relevant parameter in the system. This is reminiscent of, but different from, the case of non-Brownian suspensions [5, 6], where the phase diagram is governed by strain amplitude and density.

In marked contrast with other theoretical and experimental absorbing state systems, for which the static absorbing configurations are disordered, our system exhibits an additional ordering transition. This transition is manifested by crystallization, as indicated by the bond-orientational order parameter Ψ_6 , and is characterized by singular behavior of the density of topological defects like dislocations. To our knowledge, this is the first system where an absorbing state transition and an ordering transition occur together, each with its own distinct order parameter.

The experiment consists of a monolayer of ~ 3000 acrylic disks, each $D = 7$ mm in diameter and 3 mm thick, confined between two glass plates and subjected to oscillatory shear with maximum strain amplitude γ . To

generate the shear, the bottom wall of the cell is moved by a motorised translator stage; the side walls move about a fixed pivot connected to the top wall of the shear cell. The spacing between the plates is slightly greater than the thickness of the disks, ensuring that the disks remain in a single layer, with no buckling. The plane of the apparatus is inclined by an angle $\approx 50^\circ$ with respect to the vertical. This angle was chosen so as to be steeper than the angle at which sliding of the disks on the glass surface ensues, which we measured to be $\approx 27^\circ$. Despite this, we occasionally observe transient sticking of some disks to the plate. Lines etched on the disks may be used as fiducial markers to track the rotation of the disks.

A given run consists of many shear cycles $(i) \rightarrow (ii) \rightarrow (iii) \rightarrow (iv) \rightarrow (iv) \rightarrow (i)$ as shown in Fig. 1. During a cycle, the system is photographed by an array of raspberry pi cameras with spatial resolution 7 pixels/mm. We associate the configuration (i) with the zero phase of the oscillatory drive. Unless explicitly stated, when we refer to “strobed” images, we mean photographs taken at this zero phase condition. Before changing the strain value for a new run, the shear cell is brought horizontal to the ground and shaken, so as to erase all memory of the previous shear cycles.

Before focusing on the dependence on height, let us study the active to absorbing transition by considering measures defined on the entire system. We consider a disk to be active if it does not return to the same position at the end of a cycle. Our measure of activity will be the fraction α of currently active disks, which can thus be measured directly by comparing images taken at the beginning and at the end of a shear cycle. For the first few shear cycles, α is large, since the configurations start out random, but it decreases in an exponential manner as the system self-organizes. This is seen in Fig. 2(a), where α is plotted as a function of time, measured in shear cycles, for various strains; from these data a characteristic time τ_A is extracted for each strain. This is plotted in Fig. 2(b), which shows a divergence at a critical value of the strain, $\gamma_c \approx 0.065$. This is the first indication of a dynamical phase transition.

As noted earlier, in addition to the absorbing state transition, there is an ordering transition as a function of strain. Fig. 3(a) shows Voronoi constructions of several typical configurations, at different strains, taken after the system has reached steady state. We identify defects as Voronoi cells with more or fewer than six edges. The system has a tendency to order in a triangular lattice (which yield hexagonal Voronoi cells), and the density ρ_D of these defects tracks the crystalline order. Moreover, the bond-orientational order parameter Ψ_6 is maximal at γ_c ; see SI.

The dependence of ρ_D on the shear cycle number for several strain values is shown in Fig. 2(c), from which we can extract a γ -dependent characteristic time, τ_D . This is plotted as a function of strain in Fig. 2(d), showing a divergence. Comparing the dependence of the activity, Fig. 2(b) on the number of shear cycles, with that of the

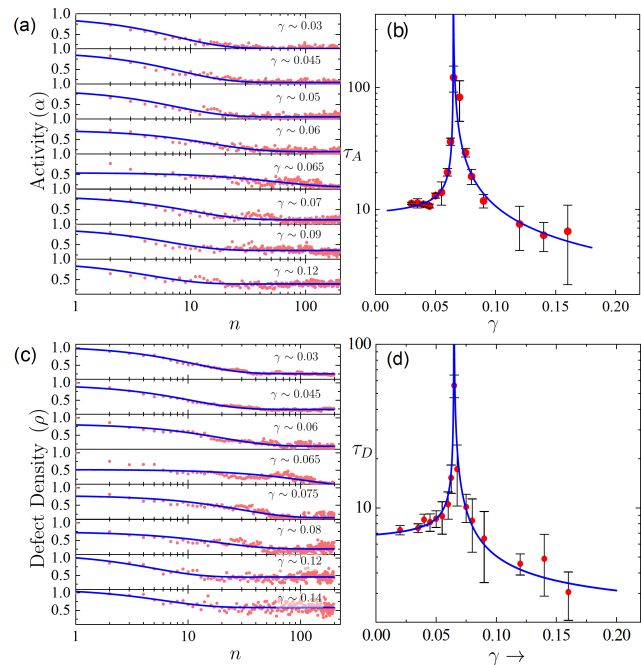


FIG. 2. (a) Dependence of the activity α on the time (in number n of shear cycles); panel (c) shows the corresponding dependence of the defect density ρ_D . The data in (a) and (c) are fitted with two exponential fits: $\alpha = (1 - \alpha_s) \exp(-n/\tau_A) + \alpha_s$ and $\rho_D = (1 - \rho_{Ds}) \exp(-n/\tau_D) + \rho_{Ds}$, which are indicated by the blue lines in the panels. In (b) and (d) we plot the dependence of the characteristic shear cycle numbers τ_A and τ_D , respectively, as a function of strain γ . In both cases, the characteristic value of shear cycle required to reach a steady state show a divergence of the form $|\gamma - \gamma_c|^{-\nu}$ with $\gamma_c \sim 0.65$ and $\nu \sim 3/4$ for both.

defect density in Fig. 2(d), we see that the ordering and the absorbing transitions occur at the same value of γ_c . In both cases there is similar dependence on the characteristic times for ordering, with both diverging at γ_c as $|\gamma - \gamma_c|^{-\nu}$ with $\nu \sim 3/4$, suggesting that the two transitions are coupled. We note that the exponent we measure is very different from that of the Conserved Directed Percolation (Manna) Class, for which $\nu \approx 1.225$ [1].

For $\gamma < \gamma_c$, the defects migrate together to form grain boundaries, as seen in Fig. 3(a), while more isolated defects and the clusters of defects are seen at higher γ . We note that existence of defects is not a direct indicator of activity, which is a question of recurrent trajectories. In Fig. 3(b), the density of defects is plotted against strain, and shows a cusp-like minimum at γ_c : $\rho_D \sim |\gamma - \gamma_c|^\beta$, with $\beta \sim 1/3$ (Ψ_6 also shows a cusp-like maximum; see SI.). We emphasize that these data were taken for systems which were initially disordered. When the system begins in an ordered lattice, it maintains its order for all but the highest strains studied, as shown by the hollow blue markers in Fig. 3(b). We note that such dependence on initial states has been seen in other absorbing state

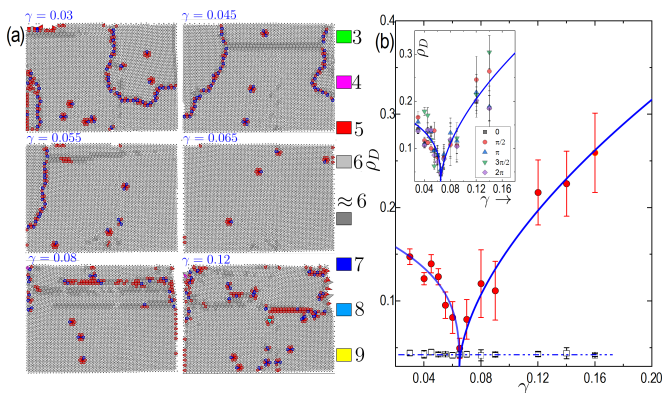


FIG. 3. (a) Characteristic snapshots of the system showing the positions of defects in the hexagonal packing, for several values of strain γ . The images are taken at the zero position in the cycle (see Fig. 1). (b) Variation of the defect density ρ_D as a function of γ . Solid red circles are for steady states obtained starting from a disordered configuration, for which a cusp-like dip in ρ_D is seen, suggesting a second-order type transition. The blue lines represent the function $\rho_D \sim |\gamma - \gamma_c|^\beta$, where $\beta \sim 1/3$. The hollow blue squares are for runs starting from an ordered state, for which there is no appreciable defect buildup. Inset: ρ_D vs γ as measured at different stages of the strain cycle. In all these cases, the initial state was disordered.

models [25] - that is, specially chosen initial states can produce final states with different statistical characteristics than those resulting from random initial states.

The collective behavior described above has direct counterparts in the individual particle trajectories. For small strains, one might expect that the particle trajectories simply move back and forth in a time-reversal invariant manner. In fact, this is not the case. Reminiscent of the trajectories seen in computer simulations of fric-

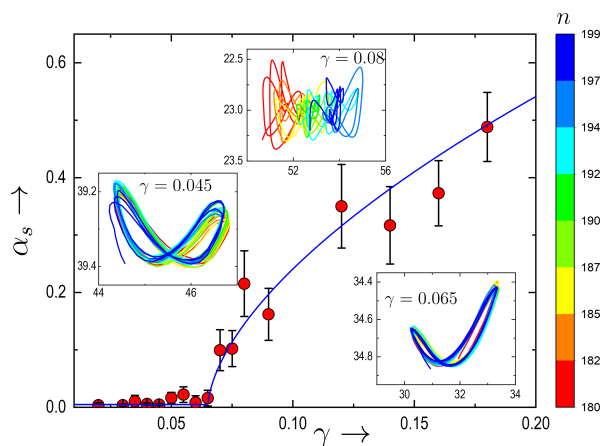


FIG. 4. Saturation activity α_s of the system as a function of strain γ . We find $\alpha_s = 0$ for $\gamma \leq \gamma_c$, and $\alpha_s \sim |\gamma - \gamma_c|^{0.6}$ for $\gamma > \gamma_c$. Typical particle trajectories are shown in the inset for three values of γ , one above, one below, and one equal to γ_c . The colors indicate the time as measured in strain cycles.

tional spheres in three dimensions [23], we see that the trajectories form closed loops, as seen in Fig. 4. In the absorbing phase, $\gamma < \gamma_c$, the loops are figure-8 shaped, remaining so until γ_c , while in the active phase the disks diffuse. In the SI we present snapshots of particle trajectories over the entire system, showing a clear left-right asymmetry, as well as the differences in trajectories near to and far from the side walls.

The dependence on height is seen in Fig. 5(a), which depicts the overlap of the configuration over time, having passed through an initial transient period during which the system organizes. The color bar indicates the amount of overlap of successive strobed images as a function of the shear cycles, averaged over all the particles at the same height. Data is shown for 50 cycles. The bottom portions of the images are dark blue, indicating that these areas are recurrent - successive strobed images overlap almost perfectly over the course of many cycles. These images show the essence of the system: For small γ , essentially all the disks return to the same positions at the zero phase point of the cycles, having traced out closed loops as seen in Fig. 4. As γ is increased, the system destabilizes from the top down - disks in the upper portion of the system no longer return, but those lower down do. For still larger γ , very few of the disks return, with their trajectories being diffusive.

Fig. 5(a) shows the average activity at depths ℓ as a function of the shear cycles n , for different strains γ . For $\gamma < \gamma_c \approx 0.065$, we see that essentially the entire system is recurrent. Above γ_c there is an increase in activity beginning at the top of the system. We suggest that for a given depth, there is some value of the strain such that disks at and above that depth will not be recurrent, but those beneath will be. This interpretation suggests that $\gamma \approx 0.065$ is the critical shear corresponding to the weight of one layer of disks.

A heuristic argument for the reason behind the dependence of average activity on depth can be made as follows. Consider a typical row at depth ℓ . When the system is strained, the row of disks is compressed by an amount proportional to γ . This produces a stress on the disks which itself is proportional to γ . This stress will have an upward component on some of the disks in the row, which is resisted by the downward pressure due to the disks above it. When the upward stress exceeds the pressure, the disks will rise. In a coarse-grained sense, the stress at depth ℓ will scale as $G\gamma - \rho g \ell$, where G is an effective elastic modulus, ρ is the mass density of the disk configuration (roughly the disk mass times the area fraction), and g is the gravitational acceleration, so that $\rho g \ell$ is the pressure on the layer. We have neglected friction with the back plate since it is inclined more than the angle of repose. When $G\gamma \gtrsim \rho g \ell$, some disks will displace. A fraction of these disks will not return to their initial positions, resulting in activity. γ_c , then, would be the strain required to distort the top layer, for which $\ell \sim$ one disk diameter.

Fig. 5(b) shows the minimum depth where the activ-

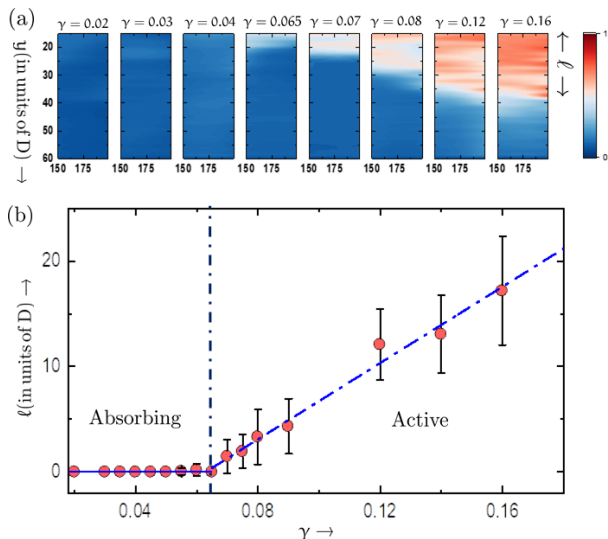


FIG. 5. (a) Average activity *vs* depth for several values of strain during a time window spanning 50 cycles. Blue indicates no or small activity, red indicates high activity. For each of the panels, the activity is estimated by subtracting successive strobed images, and averaging over slices at each height (See SI). Thus, we see that the lower portion of all the systems is recurrent, and that the active region at the top increases in size as γ increases above γ_c . No activity is observed for $\gamma < \gamma_c$. (b) The depth of the active region (in units of disk diameter), plotted as a function of γ . The dashed line is what might be expected, as discussed in the text.

ity is zero. For small strain, $\gamma < \gamma_c \approx 0.065$, this is zero, since the entire system is inactive. Above this strain, the upper portion of the configuration becomes active, with depth increasing as strain increases. Effectively, Fig. 5(b) depicts the phase diagram of the system - if we interpret the depth as being pressure, then the portion above the curve is the absorbing phase where the system is recurrent, and below the curve it is active. We expect, given that contacts with the side walls are continually being broken, that little of the weight is taken up by friction with the side walls, so the pressure should be a linear function of depth. This picture is complimented by the images of particle trajectories shown in

the SI. Below the relevant critical height, the trajectories form (comparatively) tight orbits, giving way to increasingly fuzzy and then diffuse paths as we look higher and higher.

Last, we turn to the question of disk rotation. We have etched lines on the disks, which allows us to follow the rotation of the individual disks. The rotational motion of a disk behaves like a biased random walk, with an angle ϕ behaving as $\frac{d\phi}{dt} = \omega + \eta(t)$. That is, the particle rotates with an average angular velocity ω , augmented by a noise term η . Roughly half the particles rotate in a clockwise fashion ($\omega < 0$), and the rest counterclockwise ($\omega > 0$). As seen in the SI, for $\gamma \leq \gamma_c$, the maximum ω value found is approximately the same. As γ increases past γ_c , the maximum ω increases. Clockwise and counterclockwise rotators are distributed throughout the system, as is expected for frictional systems (think of interlocking gears), but a preponderance of one chirality or the other is seen at the side walls.

We have studied a cyclically driven system of disks in two dimensions, with maximum strain acting as the control parameter. Defining an active particle as one which does not return to its initial position at the end of a drive cycle, we find that there is a well-defined active-absorbing phase transition. We note, however, that the transition does not appear to be of the Conserved Directed Percolation (Manna) class [1]. This may be because there is an additional ordering field in the problem. In the typical CDP class, there is no spatial symmetry breaking involved, as both absorbing and active states are disordered. Because the disks are monodisperse, they have a natural tendency to crystallize in a triangular lattice. It is known that the addition of a second conservation law can change the nature of these states [26], and we may speculate that the addition of an ordering field may play an analogous role.

We acknowledge support of the Department of Atomic Energy and Science & Engineering Research Board, Government of India, under Projects 12-R&D-TFR-5.10-0100 and CRG/2020/000507. DL thanks the Israel Science Foundation (Grant No. 1866/16) and the U.S.-Israel Binational Science Foundation (Grant No. 2014713). PMC acknowledges support from DOE BES under grant No. DE SC0020976 for modeling and data analysis.

-
- [1] M. Henkel, H. Hinrichsen, and S. Lübeck, *Non-Equilibrium Phase Transitions - Volume 1: Absorbing Phase Transitions* (Springer, 2008).
- [2] H. Hinrichsen, Non-equilibrium critical phenomena and phase transitions into absorbing states, *Advances in Physics* **49**, 815 (2000).
- [3] S. Torquato and F. H. Stillinger, Local density fluctuations, hyperuniformity, and order metrics, *Physical Review E* **68**, 041113 (2003).
- [4] D. Hexner and D. Levine, Hyperuniformity of critical absorbing states, *Physical Review Letters* **114**, 110602 (2015).
- [5] D. J. Pine, J. P. Gollub, J. F. Brady, and A. M. Leshansky, Chaos and threshold for irreversibility in sheared suspensions, *Nature* **438**, 997 (2005).
- [6] L. Corte, P. Chaikin, J. P. Gollub, and D. Pine, Random organization in periodically driven systems, *Nature Physics* **4**, 420 (2008).
- [7] S. Wilken, R. E. Guerra, D. J. Pine, and P. M. Chaikin, Hyperuniform structures formed by shearing colloidal suspensions, *Physical Review Letters* **125**, 148001 (2020).
- [8] J. Ren, J. A. Dijksman, and R. P. Behringer, *Reynolds*

- pressure and relaxation in a sheared granular system, *Physical review letters* **110**, 018302 (2013).
- [9] I. Regev, J. Weber, C. Reichhardt, K. A. Dahmen, and T. Lookman, Reversibility and criticality in amorphous solids, *Nature communications* **6**, 8805 (2015).
- [10] T. Kawasaki and L. Berthier, Macroscopic yielding in jammed solids is accompanied by a nonequilibrium first-order transition in particle trajectories, *Physical Review E* **94**, 022615 (2016).
- [11] H. Bhaumik, G. Foffi, and S. Sastry, The role of annealing in determining the yielding behavior of glasses under cyclic shear deformation, *Proceedings of the National Academy of Sciences* **118** (2021).
- [12] P. Leishangthem, A. D. Parmar, and S. Sastry, The yielding transition in amorphous solids under oscillatory shear deformation, *Nature communications* **8**, 1 (2017).
- [13] A. D. Parmar, S. Kumar, and S. Sastry, Strain localization above the yielding point in cyclically deformed glasses, *Physical Review X* **9**, 021018 (2019).
- [14] D. Fiocco, G. Foffi, and S. Sastry, Encoding of memory in sheared amorphous solids, *Physical review letters* **112**, 025702 (2014).
- [15] S. Mukherji, N. Kandula, A. Sood, and R. Ganapathy, Strength of mechanical memories is maximal at the yield point of a soft glass, *Physical review letters* **122**, 158001 (2019).
- [16] J. D. Paulsen, N. C. Keim, and S. R. Nagel, Multiple transient memories in experiments on sheared non-brownian suspensions, *Physical review letters* **113**, 068301 (2014).
- [17] C. Ness and M. E. Cates, Absorbing-state transitions in granular materials close to jamming, *Physical review letters* **124**, 088004 (2020).
- [18] N. Mangan, C. Reichhardt, and C. O. Reichhardt, Reversible to irreversible flow transition in periodically driven vortices, *Physical review letters* **100**, 187002 (2008).
- [19] C. Reichhardt and C. Reichhardt, Reversible to irreversible transitions for cyclically driven disks on periodic obstacle arrays, *arXiv preprint arXiv:2202.05384* (2022).
- [20] W.-T. Yeh, M. Ozawa, K. Miyazaki, T. Kawasaki, and L. Berthier, Glass stability changes the nature of yielding under oscillatory shear, *Physical review letters* **124**, 225502 (2020).
- [21] M. Mungan and S. Sastry, Metastability as a mechanism for yielding in amorphous solids under cyclic shear, *Physical review letters* **127**, 248002 (2021).
- [22] I. Regev, T. Lookman, and C. Reichhardt, Onset of irreversibility and chaos in amorphous solids under periodic shear, *Physical Review E* **88**, 062401 (2013).
- [23] J. R. Royer and P. M. Chaikin, Precisely cyclic sand: Self-organization of periodically sheared frictional grains, *Proceedings of the National Academy of Sciences* **112**, 49 (2015).
- [24] We note that this is true in a coarse-grained sense. On a grain scale, we expect force chains, although because of the continual shearing, these should be rather short in extent and in temporal duration.
- [25] D. Hexner, P. M. Chaikin, and D. Levine, Enhanced hyperuniformity from random reorganization, *Proceedings of the National Academy of Sciences* **114**, 4294 (2017).
- [26] D. Hexner and D. Levine, Noise, diffusion, and hyperuniformity, *Physical Review Letters* **118**, 020601 (2017).

Supplementary Material: Coupled dynamical phase transitions in driven disk packings

Akash Ghosh,¹ Jaikumar Radhakrishnan,² Paul Chaikin,³ Dov Levine,⁴ and Shankar Ghosh⁵

¹*Dept. of Condensed Matter Physics and Materials Science,
Tata Institute of Fundamental Research, Mumbai 400005, India*

²*School of Technology and Computer Science, Tata Institute of Fundamental Research, Mumbai 400 005, India*

³*Center for Soft Matter Research and Department of Physics, New York University, New York, NY 10003*

⁴*Department of Physics, Technion-IIT, Haifa 32000, Israel*

⁵*Department of Condensed Matter Physics and Materials Science,
Tata Institute of Fundamental Research, Mumbai 400005, India*

(Dated: March 15, 2022)

I. EXPERIMENTAL DETAILS

To construct the trajectory of a system of N disks, two tasks need to be accomplished. First, centers of the disks must be identified in each image. This is used to generate a list of positions $P_t(\mathbf{r}_1, \mathbf{r}_2, \dots, \mathbf{r}_N)$ for every instance of time t . Here, $\mathbf{r}_i(t) \equiv (x_i(t), y_i(t))$ is the position vector associated with the center (x_i, y_i) of the i^{th} disk. Second, a correspondence needs to be established between the entries of a list P_{t_1} at time t_1 to the entries of a different list P_{t_2} at time t_2 .

Procedures to generate this linked list rely on optimizing a suitable cost function that is associated with different possible associations that can be realized across adjacent lists [1]. For large number of particles this method becomes highly complex due to the growing combinatorics. To reduce the complexity, we used two colored disks, orange and blue. Both of these are made of acrylic and are the same size (7 mm in diameter and 3 mm thick), shape and frictional properties.

Detecting the center of the disks

To detect the centers of the disks with sufficient spatial resolution, it is necessary to use an imaging system that has (i) a large field of view, (ii) high spatial resolution and (iii) low image distortion. Single camera systems (of the non-telecentric type) that have large field of view are also associated with parallax errors [2]. In the context of our experiments, it would mean that the disks appear as circles only at the center of the image, towards the edge of the image the side walls of the disks become visible. Parallax error of this type generates systematic errors in the detection of the disk's center.

Image stitching

To achieve the requirements of the imaging we used two raspberry pi cameras, each with spatial resolution 7 pixels/mm. The cameras are so positioned that one camera images the left part of the system while the other camera images the right part. The central part of the system is imaged by both the cameras. This common

part is used to stitch the images into one composite RGB image, I_{RGB} . The imaging is done using the functions of the OpenCV stitcher class [3]. Representative images captured by the two cameras and the obtained stitched image is shown in Fig. S1. Please note that the stitching is not seamless due to which an excess vertical array of defects is often seen in the middle of the image.

Image processing:

As part of constructing the trajectories of the disks, we follow the process given below

- We separate the stitched RGB image I_{RGB} into three channels; the red channel I_R reveals the orange disks, whereas the blue channel I_B shows the blue disks. We use the green channel I_G data for normalising the intensity.
- These images I_R and I_B are then converted into their corresponding binary images, B_R and B_B . In these binary images the disks appear as white and the interstitial space between them appear as black. We use back-light illumination, this helps in enhancing the contrast between the white background and the colored disks.
- These binary images are then inverted, such that in the inverted image \bar{B}_R the orange disks appear as black and the interstitial space appears as white.
- We then use Pythagorean distance transform [4] on these inverted binary images \bar{B}_R and \bar{B}_B which creates the distance matrices D_R and D_B by assigning to each pixel in $D_R(i, j)$ and $D_B(i, j)$ the value of the Pythagorean distance between the (i, j) pixel and the nearest white pixel in \bar{B}_R and \bar{B}_B , respectively. Thus, the white interstitial space in \bar{B}_R is assigned to zero in D_R and the black pixels \bar{B}_R are assigned to non zero values in D_R . Center of the disk is the farthest point from the nearest white pixels and hence have the maximum value.
- We search for local maxima in the distance matrix D to find the list of the centers of the disks. These two lists, one for the orange disks and the other

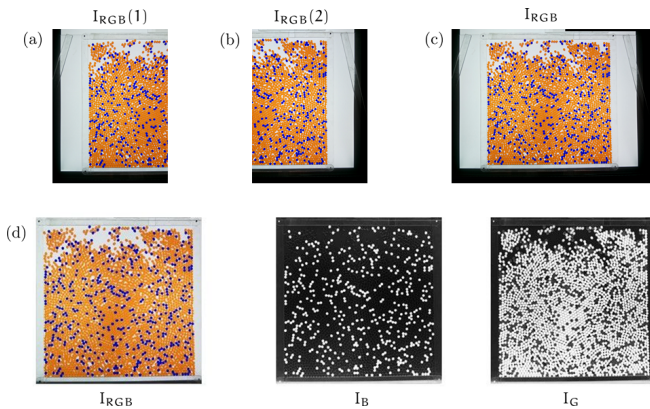


FIG. S1. **Experimental Details:** The images $I_{\text{RGB}}(1)$ (a) and $I_{\text{RGB}}(2)$ (b) of the system is photographed by 2 raspberry pi cameras, each with spatial resolution 7 pixels/mm. These images are then stitched using the functions of the openCV stitcher class. The stitched images are shown as I_{RGB} in panel (c). Both orange and blue disks are made of acrylic and are of the same size and shape. As part of the tracking process, we separated the stitched RGB image I_{RGB} into three channels, the red channel I_{R} reveals the orange disks, whereas the blue channel I_{B} shows the blue disks. We use the green channel data for normalising the intensity. Having the images partitioned into red and blue helps reduce the complexity associated with the combinatorics involved in tracking the particles.

for the blue disks are concatenated to generate the complete position list $P(\mathbf{r}_1, \mathbf{r}_2, \dots, \mathbf{r}_N)$ of the disks.

II. TRAJECTORIES

In our experiments, we monitored the trajectories of each of the disks over many shear cycles. The shear is cyclic, and we want to follow motion of the disks in different cycles. To this end, we denote the position of the i^{th} disk at time t in the n^{th} cycle by $\mathbf{r}_{i,n}(t) = (x_{i,n}(t), y_{i,n}(t))$, where (x, y) are the in-plane coordinates of the center of a disk, and t runs over the duration of a single cycle. By etching a line on each disk, we were able to follow their angular orientations. Typical particle trajectories are shown in Fig. S2 for representative values of γ . The colors indicate the shear cycles. For small γ , the trajectories start out random, and gradually tighten into clearly repetitive motion. On the other hand, for large γ , the trajectories do not settle down, suggesting that if we were to follow them long enough they would show broadly diffusive behavior.

In Fig. S3 we explore the handedness of the loops associated with the trajectories and plot paths traced out by three representative particles, one near the left wall, one at the center and the other near the right wall of the shear cell. The trajectories are plotted for a representative shear cycle. The shear cycle starts from the “zero position” (i), moving to the rightmost position (ii), returning to the central position (iii), then mov-

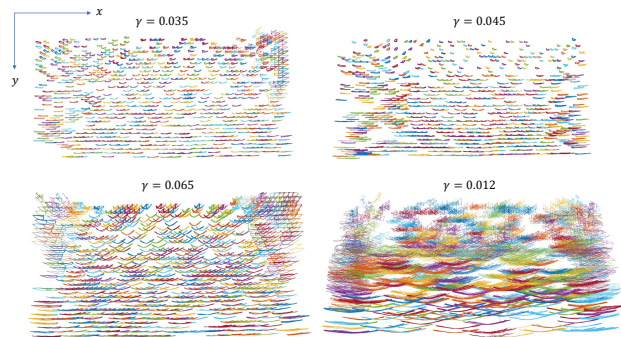


FIG. S2. **Trajectories:** The figure plots representative trajectories of disks for different strains γ . For $\gamma = 0.035, \gamma = 0.045$ and $\gamma = 0.065$ particle trajectories show loop like structures whereas for $\gamma = 0.12$ the trajectories are diffusive in nature.

ing on to the leftmost position (iv) before finally coming back to the zero position. Portion of the trajectory that corresponds to the movement of the shear cell from (i) \rightarrow (ii) is colored in blue. The next part of the trajectory (ii) \rightarrow (iii) is in magenta, the third part (iii) \rightarrow (iv) is in green and the last part (iv) \rightarrow (i) that completes the shear cycle is marked red. The particle near the left wall of the shear cell undergoes a clockwise motion while those near the right wall undergo an anticlockwise motion. Particles in the center, show ∞ -shaped loops. These particles transit from clockwise to anticlockwise motion and vice versa during the shear cycle.

a. Cumulative mean square displacement Figure S4 shows the cumulative mean square displacement (CMSD) as a function of cycle number n :

$$\Delta^2 = \langle r^2(n - n_0) \rangle - \langle r(n - n_0) \rangle^2 \quad (1)$$

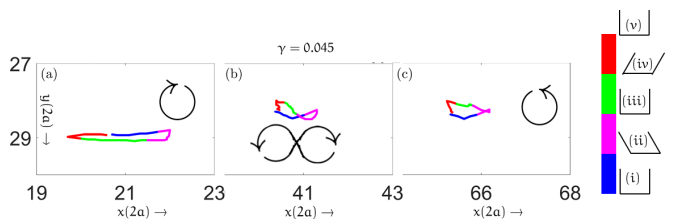


FIG. S3. **Handedness of the trajectories** The figure plots trajectories of a single shear cycle for three representative particles, one near the left wall of the shear cell (a), one at its center (b) and the other near its right wall (c). Portion of the trajectory that corresponds to the movement of the shear cell from (i) \rightarrow (ii) is colored in blue. The next part of the trajectory (ii) \rightarrow (iii) is in magenta, the third part (iii) \rightarrow (iv) is in green and the last part (iv) \rightarrow (i) that completes the shear cycle is marked red. The particle near the left wall of the shear cell undergoes a clockwise motion while those near the right wall undergo an anticlockwise motion. Those that are in the center, show ∞ -shaped loops. These particles transit from clockwise to anticlockwise motion and vice versa during the shear cycle.

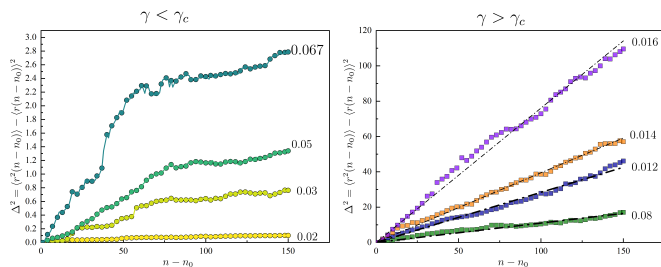


FIG. S4. **Cumulative mean square displacement (CMSD):**The figure shows the cumulative mean square displacement (CMSD) as a function of cycle number n . The CMSD is defined as $\Delta^2 = \langle r^2(n - n_0) \rangle - \langle r(n - n_0) \rangle^2$, where the positions are sampled at the end of each cycle n , and the sum is over all the disks. For strains above $\gamma_c = 0.065$, the CMSD diverges with time (right panel), while for $\gamma < \gamma_c$ it tends to be a constant(left panel).

where the positions are sampled at the end of each cycle, $t = T$, and the sum is over all the disks, N in number. For values of strain γ that is smaller than γ_c the CMSD Δ^2 saturates with increasing cycle number. However, for values of $\gamma > \gamma_c$, the dynamics of the disks becomes diffusive and CMSD grows almost linearly with n . For $\gamma = 0.02, \gamma = 0.04$ and $\gamma = 0.065$ particle trajectories show loop like structures whereas for $\gamma = 0.14$ the trajectories are diffusive in nature.

III. MEASUREMENT OF ACTIVITY

A. From the trajectories

The activity α of the system measured in the n^{th} shearing cycle physically means the fraction of disks which do not return to the position occupied by it at the beginning of the n^{th} cycle. This is measured by computing the residual displacement $\varepsilon_i^n = d_i^n$, where d_i^n is the distance between the coordinates of a disk associated with its position at the beginning and end of each shear cycle. If this residual displacement ε_i^n is greater than a tolerance value (chosen to be 0.25 times the diameter of the disk), we consider that the particle has not returned to its earlier configuration and hence is an active particle. The activity α is given by the number of active disks normalized by the total number of disks in the system.

Spatial regions containing the active particles are referred to as active regions. To estimate the spatial structure of the active region in the system we performed two analysis. The first method consisted of overlaying the position of the detected particles in the strobed condition - for which the phase of the shear cycle is zero. This overlay is done for the last few shear cycles. In the second method we analysed the difference matrix obtained by subtracting two strobed images from subsequent shear cycles.

B. From strobed positions

Let $P_n((x_1, y_1), (x_2, y_2), \dots, (x_N, y_N))$ be the set of coordinates of the disks in the strobed condition (phase of the stain cycle is zero) for the n^{th} cycle. We generate a larger set of points \mathcal{P} by taking the union of these sets from different strain cycles $\mathcal{P} = \bigcup_{n=m}^{m'} P_i$, here m and m' represent the two ends of the interval $[m, m + 1, \dots, m']$ of strain cycles which is considered in constructing the set \mathcal{P} . If the system returns to its previous position at the end of each strain cycle, then the cardinality of the set \mathcal{P} equals that of the individual position sets P_n . However, if there is activity in the system, the cardinality $|\mathcal{P}|$ increases with the size of the interval, $m' - m$. A visual inspection of scatter plot of all the points in the set \mathcal{P} is highly instructive in uncovering the spatial structure associated with active regions. Representative scatter plots of the points in \mathcal{P} for different values of strain γ is plotted in Fig. S5. The scatter plot is localised in non-active parts, whereas it is smeared in the active zone. For small values of γ , the entire system is non-active. However, beyond a critical strain, the top part of the system becomes active. This is the regions where the scatter plots get smudged. The extent of smudging grows as the amount of strain increases.

C. From the strobed images

From the set of the images that were taken during the experiment we formed a list of strobed images $I(n)$, one taken at a predefined phase from each shear cycle. Here, n is the shear cycles number. An estimate of the activity in the system can be evaluated by taking the difference between two consecutive strobed images $\delta I_{(x,y)}(n) = |I_{(x,y)}(n) - I_{(x,y)}(n + 1)|$ (see Fig.S6(a)). Elements of the matrix $\delta I_{(x,y)}(n)$ whose value is beyond a threshold value is considered to be active. We find

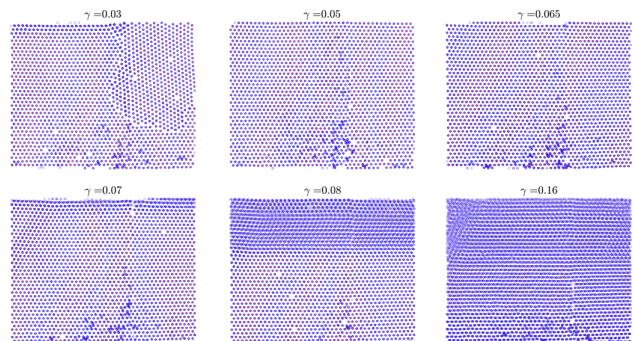


FIG. S5. Representative scatter plots of the points in the set $\mathcal{P} = \bigcup_{n=190}^{200} P_i$ for representative values of the strain γ . Here $P_n((x_1, y_1), (x_2, y_2), \dots, (x_N, y_N))$ is the set of coordinates of the disks in the strobed condition in the n^{th} strain cycle. Please note that the vertical array of defects that one sees at the middle is an artifact of image stitching.

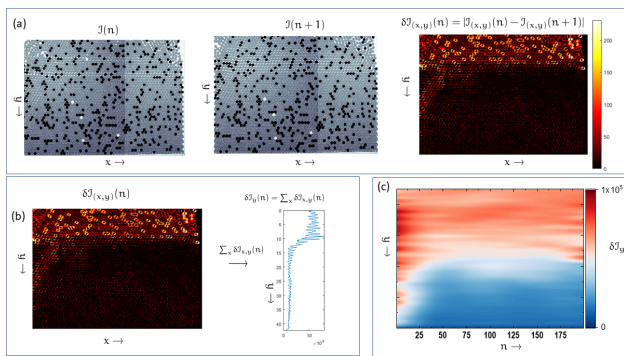


FIG. S6. (a) The left and the center panels show strobed images for two consecutive strain cycles ($n=150$ and $n=151$ for $\gamma = 0.08$). The right panel shows the difference between these two images, $\delta I_{(x,y)}(n) = |I_{(x,y)}(n) - I_{(x,y)}(n+1)|$. The colorbar represents the magnitude of this difference. (b) The difference matrix $\delta I_{(x,y)}(n)$ is then summed over the columns to give a column vector $\delta I_y(n) = \sum_x \delta I_{x,y}(n)$. This is done for all values of n , as a result we obtain n column vectors $\delta I_y(n)$. (c) These column vectors are then concatenated to generate the matrix $\delta \mathcal{I} = (\delta I_y(1)|\delta I_y(2)| \dots |\delta I_y(n)|\delta I_y(n+1) \dots)$.

that these active regions are mostly localised near the free surface, while the region close to the bottom wall is non-active.

To study the growth and organisation of the active region in the system as a function of the shear cycle number, we first convert the matrix $\delta I_{(x,y)}(n)$ to a column vector $\delta I_y(n)$ by summing over the columns.

$$\delta I_y(n) = \sum_x \delta I_{x,y}(n).$$

The intensity profile $\delta I_y(n)$, represents the variation of the average activity as a function of height (see Fig.S6(b)). Having obtained the average activity profile as a function of height for a given value of n , we concatenate $\delta I_y(n)$ arrays vertically for increasing values of n and

$$\delta \mathcal{I} = (\delta I_y(1)|\delta I_y(2)| \dots |\delta I_y(n)|\delta I_y(n+1) \dots).$$

This matrix is plotted in Fig.S6(c). The blue regions correspond to the periodic part of the dynamics (non-active region, here after each cycle particles return to starting position). On the other hand we have the red region where the particles are active.

IV. QUANTIFYING ORDER

We used both voronoi construction and bond orientation order parameter ψ_6 to estimate the amount of disorder in the system.

a. Voronoi Construction: The voronoi edges are perpendicular bisectors to adjacent sites and hence the voronoi cell is a convex polygon. Since the number of

edges n_E of a polygon are same as the number of its adjacent sites, we associate n_E with the coordination number of the point that is contained inside the cell. Here each point corresponds to the center of a disk. In two dimension, a crystal lattice is associated with six nearest neighbours. Therefore, the voronoi cells with edges not equal to six are considered as defects. However, there are a lot of irregular hexagons associated with configurations generated by slipping of one particle layer over another. Although these hexagons have six edges, they don't correspond to a crystal and we count them as defects. The irregularities of the hexagons are defined by the ratio of length of the longest edge to length of the shortest edge of the voronoi cell. If the ratio is more than 3.5, the corresponding hexagon is considered as a defect.

b. Bond orientation parameter: The extent of local order of the i^{th} particle and its N_i nearest neighbors is estimated from the single particle bond orientation parameter, $q_6(i) = \frac{1}{N_i} \sum_{j=1}^{N_i} e^{i6\theta_{ij}}$. Where θ_{ij} is the angle between the center-to-center vector from particle i to j around a fixed arbitrary axis. In the perfect crystalline environment $q_6(i) = 1$. The degree of crystallinity decreases with increasing values of γ . An estimate of the degree of crystallinity for an entire configuration was quantified via the bond orientation order parameter ψ_6 in the following way: $\psi_6 = \langle |q_6(i)|^2 \rangle$. The Fig.S7 shows the variation of the parameter ψ_6 with γ . The value of ψ_6 is maximum as $\gamma=0.065$ indicating that the system is most crystalline for that parameter of strain.

V. ROTATION OF THE DISCS

We now describe the angular variable associated with the disks. To do so we keep track of the cumulative angular displacement of the disks. For large values of n if the disks pick up a positive cumulative angle, its trajectory, $C_i(n) = \sum_n \varphi_n^i$ is coloured red. However, if it picks up a negative cumulative angle the associated trajectory is marked blue. The angles are measured for the $\vartheta = 0$ position (central position) of the shearing cycle. In the top panel of Fig.S8 we plot the cumulative rotation of each particle with the number of shear cycles n for different values of strain amplitude. With increasing value of n , the red and the blue trajectories progressively move away from each other. The shear cycle creates a partitioning of the disks into the clockwise (blue) and the anticlockwise (red) rotating disks (see the bottom panel of Fig.S8).

The persistence of rotation of the disks comes from the following argument that holds true for all dry granular systems that are subjected to the form of shearing used in this experiment. As the two side walls ad and bc synchronously move so as to increase the shearing angle, one of the side walls become the pusher and moves the disks while the other wall (confining wall) occasionally moves ahead of the disks creating a gap. This void is filled stochastically by disks toppling into it. The disks near the pushing wall rotate due to the torque exerted on

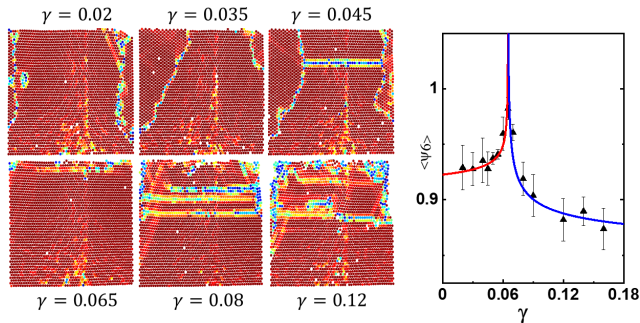


FIG. S7. (a) : The particles are color coded in the figures. The colors represent the single-particle bond orientation parameter for the i^{th} particle and its N_i nearest neighbors, $q_6(i) = \frac{1}{N_i} \sum_{j=1}^{N_i} e^{i6\theta_{ij}}$. Where θ_{ij} is the angle between the center-to-center vector from particles i to j about a fixed arbitrary axis. A particle colored in red is in the perfect crystalline environment $q_6(i) = 1$. As the color changes from red to blue the degree of crystallinity decreases. (b) : The degree of crystallinity for an entire configuration was quantified via the bond orientation order parameter ψ_6 in the following way: $\psi_6 = \langle |q_6(i)|^2 \rangle$. The figure shows the variation of the parameter ψ_6 with γ . The value of ψ_6 is maximum as $\gamma=0.065$ indicating that the system is most crystalline for that parameter of strain. The blue lines represent the function $\Psi_6 \sim |\gamma - \gamma_c|^\beta$, where $\beta \sim 1/3$. Please note that the vertical array of defects that one sees in the middle is an artifact of image stitching.

it by the boundaries while those near the confining wall rotate due to its toppling motion. Rotation is transmitted to the neighbouring disks in an opposite sense, i.e., a clockwise rotating disk imparts anti-clockwise rotation to the neighboring disks which in turn pass on a clockwise rotation to the disks in contact, this leads to geometric frustration which prevents transmission of rotational motion into the bulk. In the part of the shear cycle when the pushing side is the right side wall, the disks adjacent to it pick up an clockwise motion. Disks near the confining side wall rotate but for an entirely different reason. Since the origin of rotation is different for the disks near the pushing and pulling walls, the rotation picked up in one part of the cycle is not undone by the other part. This leads to a ratcheting motion of the disks: on an average, the disks near the left side wall are clockwise rotating while those near the right side wall rotate in a clockwise manner and as a result, the net rotation grows with n .

[1] N. Chenouard, I. Smal, F. De Chaumont, M. Maška, I. F. Sbalzarini, Y. Gong, J. Cardinale, C. Carthel, S. Coraluppi, M. Winter, *et al.*, Nature methods **11**, 281 (2014).

[2] J. Fan, J. Zhang, S. J. Maybank, and D. Tao, arXiv preprint arXiv:2011.12108 (2020).

[3] G. Bradski, Dr. Dobb's Journal of Software Tools (2000).

[4] G. Borgefors, Computer vision, graphics, and image processing **34**, 344 (1986).

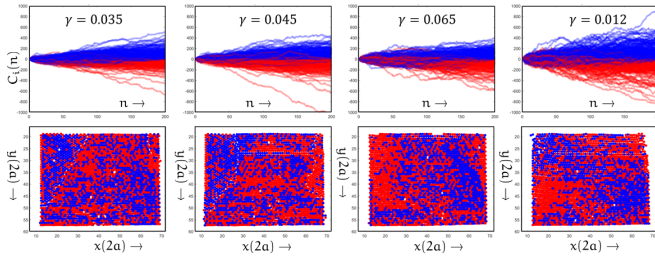


FIG. S8. **Top panel :** To describe the dynamics of the angular variable associated with the disks we keep track of the cumulative angular displacement ϑ of the disks. Here we plot the cumulative rotation of each particle with the number of shear cycles n for representative values of γ . For large values of n most disks were found to either rotate persistently in the clockwise or counter-clockwise directions. For disks that pick up a positive cumulative angle $C_i(n) = \sum_{m=1}^n \vartheta_{(i,m)}$, its trajectory, $\sum_m \varphi_{i,m}$ is coloured red. However, if it picks up a negative cumulative angle the associated trajectory is marked blue. The angles are measured for the $\vartheta = 0$ position (central position) of the shearing cycle. With increasing value of n , the red and the blue trajectories progressively move away from each other. **Bottom panel :** The figures show the spatial organization of the clock-wise and anti-clockwise rotating particles. The blue filled circles identify the clockwise rotating disks while the red filled circles identify the disks that rotate in an anti-clockwise direction. The positions of the circles correspond to the configuration attained by the disks at the end of the 200th cycle.